GHGT-12

Chimneys, channels, pathway flow or water conducting features - an explanation from numerical modelling and implications for CO_2 storage

Ludovic Räss[a]*, Viktoriya M. Yarushina[b], Nina S.C. Simon[b,c,d], Yuri Y. Podladchikov[a]

[a]University of Lausanne (UNIL), Géopolis - 1015 Lausanne, Switzerland

[b]Institute for Energy Technology (IFE), PO Box 40, 2027 Kjeller, Norway

[c]UNIK - Universitetssenteret på Kjeller, PO Box 70, 2027 Kjeller, Norway

[d]University of Oslo, PO Box 1047 Blindern 0316 Oslo, Norway

Abstract

Large amounts of CO_2 have to be captured, transported, injected and safely stored in the subsurface in order to counteract increasing atmospheric CO_2 concentrations due to steadily high consumption of energy from fossil fuels. The injection of gigatons of carbon dioxide poses challenges for pressure management and the mechanical integrity of the storage complex. Optimizing the injection strategy, controlling deformation, preventing leakage and assuring safe long term containment requires reliable and predictive hydromechanical modelling. Based on a newly derived thermodynamically consistent set of equations we have developed fully coupled codes in one, two and three dimensions. In accordance with field observations and laboratory measurements, stress dependent poro-viscoelastoplastic deformation is taken into account. Our simulations predict the spontaneous formation of self-localizing high-porosity channels (or pathway flow) under conditions applicable to CO_2 storage in reservoirs. These channels form due to mechanical instabilities that occur as a natural outcome of buoyancy driven flow in viscoplastically deforming rocks. Our results indicate that viscous deformation may explain the formation of chimneys such as those observed at the Sleipner pilot, and that non-linear effects have a major impact on the velocity and distribution of the fluid as well as on stress and deformation of the rock matrix. Thus, complex rheology and non-linear coupling between porosity, permeability, pressures and stresses should be included in state of the art reservoir simulation software in order to determine safe injection and storage conditions and correctly model observations and monitoring results.

* Corresponding author. Tel.: +41 21 69235 00; fax: +41 21 69235 05.
  E-mail address: Ludovic.Raess@unil.ch

1. Introduction

1.1. The need for numerical modeling

In order to remediate greenhouse gas emissions, enormous amounts of CO_2 need to be captured and stored underground, and correspondingly large amounts of pore space are required to accommodate the CO_2 [1]. Norway may be able to provide a significant proportion of suitable pore space in its off-shore saline aquifers and depleted oil and gas fields [2, 3]. According to EU DIRECTIVE 2009/31/EC the following requirements have to be met for transfer of responsibility from the operator of a CO_2 storage site to the authorities at site closure: 1) There is no detectable leakage; 2) the observed behaviour of the injected CO_2 conforms with the modelled behavior and 3) the site is evolving towards long-term stability. Reliable predictive models are therefore a prerequisite for industrial scale CO_2 storage. Existing reservoir simulation tools, however, are struggling to provide good predictions, in particular due to a shortage of available data [e.g., 4, 5]. The problem is likely to be aggravated for the needed very large scale storage operations (Gt of CO_2). In fact, experience with such large scale injection operations for any type of fluid is limited. CO_2 injection also differs from oil and gas operations and geothermal energy generation because injection is not (directly) balanced by withdrawal. This represents a challenge for controlling pressures and preventing unwanted deformation. Such deformation may lead to the occurrence of (felt) seismicity, surface uplift or subsidence, changes in ground water flow or CO_2 leakage out of the intended storage complex. Pressure and stress monitoring and management will therefore be crucial in large scale injection and storage operations, and correct and reliable hydromechanical models are a prerequisite. However, existing mathematical models often only qualitatively match field data or experimental results (see e.g., [6] for an extensive review on modeling of CO_2 injection and storage, and Fig. 12b in [7] for an example of modeling of experimental gas flow through shale).

1.2. The Sleipner example

One of the best documented CO_2 storage operations today is the injection of about one million tons of CO_2 per year since 1996 into the Utsira formation at Sleipner in the Norwegian North Sea. Geophysical monitoring indicates that the CO_2 is safely contained below the main cap rock and pressure at the well head is stable. Attempts have been made to history match the observations at Sleipner using conventional reservoir simulations; however, these have failed to capture first order observations, such as the facile vertical flow of CO_2 through low permeability shale layers, the formation of focused flow channels or chimneys, and rapid lateral spreading underneath the caprock shale [8]. These authors concluded that vertical CO_2 migration at Sleipner occurs "via some form of pathway flow, the pathways becoming more effective, or more numerous with time…" and stated that "The nature of these pathways is uncertain however". Such pathway flow is also frequently observed in experiments conducted on shale for nuclear waste or CO_2 storage purposes [e.g., 7, 9]. To date there are no numerical models that are able to predict the spontaneous formation and dynamic evolution of such pathways in an initially intact rock.

1.3. Localized fluid flow

In general, observations on fluid flow in the Earth's crust and in reservoirs show that fluid flow tends to be localized in space and time, requiring that permeability changes dynamically during fluid flow [e.g., 7, 8, 10, 11, 12]. Such localization is predicted from theory and experiments due to instabilities that arise as a consequence of a strong coupling between fluid flow and deformation [13-18].

1.4. Reservoir rheology

However, quantitative investigation of the potentially major effects of physical coupling of deformation and fluid flow has only recently been started [19-23]. In addition, the rheology of reservoirs may be more complex than generally assumed. Shallow reservoirs are mostly considered to behave elastically and fail by frictional plasticity. Recent experiments, however, show that reactions involving reactive fluids (as in CO_2 storage) are fast (i.e. they occur at laboratory timescales of hours to weeks) and under load lead to pressure solution and effectively viscous deformation [21, 22]. These experiments suggest that viscous deformation may play an important role in reservoirs at timescales relevant for CO_2 sequestration (days to 10000 years) and that we therefore have to consider a viscoelastoplastic rheology [24]. Even without actively flowing fluids, sedimentary rocks in reservoir and cap rock sequences deform in both brittle (elastoplastic) and ductile (viscous) manner [e.g., 25, 26, 27]. Implementation of such realistic complex rheology into the model is needed to simulate observed compaction in reservoirs [e.g., 28] and may be the key to explain the "pathway flow" observed at the Sleipner CO_2 injection site (Norwegian North Sea), and in experiments [29 and references therein]. In this contribution we will study the large scale consequences of both complex viscoelastoplastic rock rheology and the effect of non-linearity for dynamically evolving permeability in different reservoir rock types. This work is an extension of the two-dimensional (2D) results of Simon and co-workers [30-32], which were also based on the simplified assumption of a lithostatic stress state. The new model presented here includes full mechanics and therefore allows us to investigate flow and deformation in a heterogeneously stressed crust with non-linear poroviscoelastoplastic rheology.

2. Model equations

2.1. Basic formulation

A system of equations for poroviscoelastoplastic deformation and flow was derived in [18, 33]. The model gives a generalization of Biot's theory of poroelasticity to large poroviscoelastoplastic deformations, and is consistent with Gassmann's equations and the elastic effective stress law [18, 19]. The closed system of equations describing fluid flow in porous viscoelastoplastic media consists of the following minimum set of equations that represent

Mass balance

$$\frac{1}{\rho_s}\frac{d^s\rho_s}{dt} - \frac{1}{1-\varphi}\frac{d^s\varphi}{dt} + \nabla_j v_j^s = 0 \tag{1}$$

$$\frac{\varphi}{\rho_f}\frac{d^f\rho_f}{dt} + \frac{d^s\varphi}{dt} + \varphi\nabla_j v_j^s + \nabla_j q_j^D = 0 \tag{2}$$

Force balance

$$\nabla_j\left(\overline{\tau}_{ij} - \overline{p}\delta_{ij}\right) - g\overline{\rho}\hat{z}^i = 0 \tag{3}$$

$$q_i^D = -\frac{k}{\eta_f}\left(\nabla_i p^f + g\rho^f \hat{z}^i\right) \tag{4}$$

Closure relations

$$\varepsilon_{ij} = \frac{1}{2G}\frac{d^s\bar{\tau}_{ij}}{dt} + \frac{\bar{\tau}_{ij}}{2\eta_s} \tag{5}$$

$$\frac{d^s\varphi}{dt} = \frac{1}{K_\varphi}\left(\frac{d^f p^f}{dt} - \frac{d^s\bar{p}}{dt}\right) + \frac{1}{\eta_\varphi}\left(p^f - \bar{p}\right) \tag{6}$$

$$\nabla_k v_k^s = -\frac{1}{K_{dry}}\left(\frac{d^s\bar{p}}{dt} - \alpha\frac{d^f p^f}{dt}\right) - \frac{\bar{p} - p^f}{(1-\varphi)\eta_\varphi} \tag{7}$$

$$\nabla_k q_k^D = \frac{\alpha}{K_{dry}}\left(\frac{d^s\bar{p}}{dt} - \frac{1}{B}\frac{d^f p^f}{dt}\right) + \frac{\bar{p} - p^f}{(1-\varphi)\eta_\varphi} \tag{8}$$

Here, ρ^s, ρ^f are solid and rock densities, v_i^s and q_i^D are the components of solid velocity and Darcy's flux, φ is the porosity, $\bar{p}, p^f$ are the total and fluid pressures, k is the porosity-dependent permeability, $\bar{\tau}_{ij}$ are the total stress deviators, K_{dry} is the dry bulk modulus, K_φ, η_φ are the effective bulk modulus and viscosity, α is the Biot-Willis coefficient, B is the Skempton's coefficient. Equation (5) relates shear strain rates to shear total stresses in a standard Maxwell viscoelastic manner. Equation (6) shows that changes in porosity and, therefore, permeability are caused by the difference in total and fluid pressures ($\bar{p} - p^f$). Equation (7) indicates that the total volumetric deformation of the rock is driven by effective stress with a Biot-Willis factor, and that it consists of elastic (first term) and viscous (second term) contributions. We assume here that solid rock grains are elastically compressible. Equation (8) shows that the flow is affected by total pressure as well as by fluid pressure, again with elastic and viscous components. In the purely elastic limit, equations (7) and (8) reduce to Biot's classical poroelastic relations.

The model is for now restricted to one fluid phase in the pore space since our focus is on hydromechanical interactions.

2.2. Model parameters

Constitutive equations (1) – (8) have a number of material parameters that are dependent on the stress state in terms of the first and second stress invariants. Effective bulk modulus K_φ and effective viscosity η_φ were obtained using methods of effective media theory as averaged properties of the representative volume element. They depend on solid elastic and/or viscous moduli as well as on porosity

$$K_\varphi = m\frac{G_s}{\varphi}, \quad \eta_\varphi = m\frac{\eta_s}{\varphi} \tag{9}$$

where m is a geometric factor. It is equal to 1 for cylindrical pores and significantly reduces for elongated pores. Solid shear viscosity η_s is often assumed to depend on the equivalent shear stress in the following manner:

$$\eta_s = \frac{\eta_0}{1 + \left(\tau_{II}/\tau_b\right)^{N-1}} \tag{10}$$

where τ_{II} is the second stress invariant, τ_b is a breakdown stress level and N is a power-law exponent with typical value *N*=3. This expression captures non-Newtonian power-law creep rheology.

When stresses reach the yield limit, effective bulk modulus and viscosity drop significantly exhibiting a strong dependence on effective pressure and a compaction/decompaction asymmetry (Fig. 1).
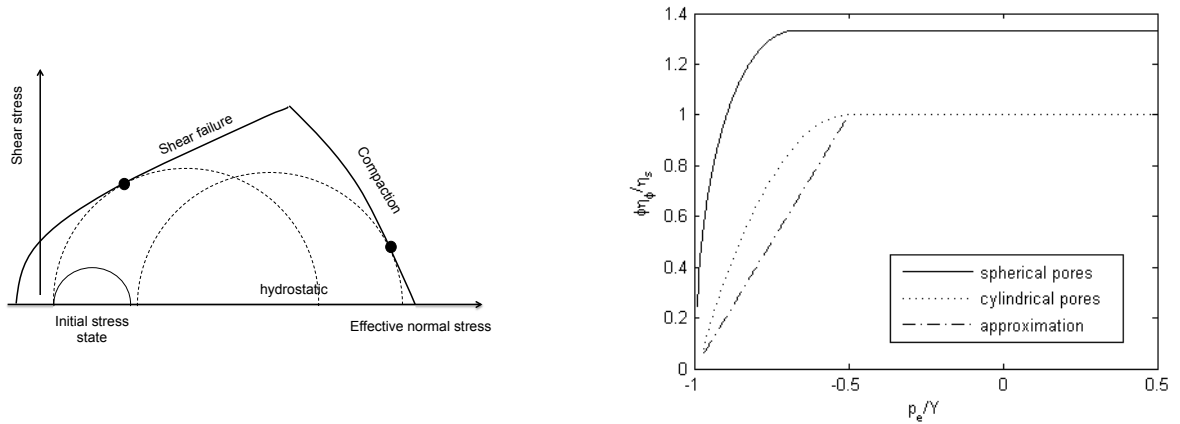

Fig. 1. (a) Failure envelope for viscoelastoplastic rocks. Inside the envelope material behaviour is viscoelastic. During injection the stress state changes from its initial state and eventually reaches shear failure or the compaction line. At this point decompaction weakening as shown on the right begins. (b) Effective viscosity η_φ of viscoplastic porous rock normalized to the shear viscosity of the solid rock frame η_s and porosity φ as a function of ratio p_e/Y of effective pressure to the yield strength *Y* of rock frame. In the compaction regime (p_e>0) effective viscosity does not depend on the effective pressure, while in the decompaction regime (p_e<0) viscosity exhibits nearly linear dependence on effective pressure after failure is initiated at $p_e = -(1-\varphi)Y/2$. At $p_e = -(1-\sqrt{\varphi})Y$ material is losing its integrity (full pore collapse) and effective pressure build up cannot be supported by the solid rock frame.

Other mechanical parameters are related to the bulk moduli K_s and K_ϕ as follows:

$$\frac{1-\varphi}{K_d} = \frac{1}{K_\varphi} + \frac{1}{K_s} \tag{11}$$

$$\alpha = 1 - \frac{K_d}{K_s} \tag{12}$$

$$B = \frac{\dfrac{1}{K_d} - \dfrac{1}{K_s}}{\dfrac{1}{K_d} - \dfrac{1}{K_s} + \varphi\left(\dfrac{1}{K_f} - \dfrac{1}{K_s}\right)} \tag{13}$$

Equation (10) is analogous to the first Gassmann's relation [18], equation (11) is a definition of the Biot-Willis coefficient, and (12) is a definition of the Skempton's coefficient [34].

Numerous laboratory measurements on fluid flow in porous rocks indicate that permeability changes during

compaction/decompaction as a function of porosity [35, 36]

$$k = k_0 \left(\varphi / \varphi_0 \right)^n \tag{14}$$

where k_0 and φ_0 are background values of the permeability and porosity, respectively. The degree to which permeability depends on porosity is controlled by exponent n. n is a material parameter, which is usually taken to be between 3 and 5 for sandstones, but can be as high as 25 for shales [35].

2.3. Flow instability and chimney formation

Poroviscoelastic equations have been previously used in the literature for modeling of melt ascend in the deep Earth [37], petroleum migration from source rocks [20] and compaction and fluid expulsion in sedimentary basins [17, 38]. One of the astonishing results of those studies is the generation of a special type of fluid flow instability that leads to the formation of high-porosity, high-permeability domains that are able to self-propagate upwards due to the interplay between buoyancy and viscous resistance of the deforming porous rock matrix. This instability was named "porosity wave" due to its resemblance to solitary waves known in fluid dynamics if porosity is plotted as a function of depth [39]. As instability, porosity waves do not form everywhere. They require special conditions to be met. A first and very important requirement is the ability of the solid rock frame to undergo time-dependent deformation such as purely viscous, viscoelastic or viscoplastic deformation.

The appearance of porosity waves strongly depends on the type of rock rheology. In viscous and viscoelastic rocks they would form more or less spherical fluid-rich blobs that propagate upwards without changing their shape (Fig. 3). Plasticity and the difference between compaction and decompaction responses lead to focusing of the porosity wave and formation of vertical self-propagating channels (Fig. 2, Fig. 5). A second requirement for the generation of porosity waves is a non-linear dependence of permeability on porosity, i.e. the exponent in the power-law for permeability (13) has to be $n > 1$. Finally, the injection rates must locally exceed the Darcy flow rate so that fluid diffusion through porous rock cannot prevent local building up of fluid pressures in the CO_2 plume.

All these conditions are likely to be met at CO_2 injection sites. Indeed, the viscous rheology of sandstones and shales comprising typical reservoirs is well documented (e.g., [40, 41]), as is the nonlinearity of porosity-dependent permeability of these rocks (e.g., [35, 36]). Therefore, upward propagation of CO_2 due to buoyancy and formation of channels is not surprising. In the following chapters, we numerically investigate the generation of porosity waves using in-house developed viscoelastoplastic numerical codes. Previous research showed that many features of three-dimensional (3D) porosity waves are captured in one-dimensional (1D) calculations, which represent vertical cross-sections of the wave.

3. Numerical implementation

A particular challenge for hydromechanical models is the issue of how to model the coupling between flow and deformation in numerical codes. These two processes are inherently coupled. However, numerical implementation of the full coupling is challenging and computationally expensive. Numerical modelling attempts are therefore largely restricted to one-way sequential coupling of two different codes (e.g. TOUGH-FLAC [6, 42]) where large number of iterations are required for accurate predictions [43].

Iterative solving of the non-linear problem, however, may not be sufficient to capture the strong physical couplings between flow and deformation that are a main feature of the thermodynamically consistent system of equations, and linear elastic behaviour is clearly an oversimplification of the behaviour of porous reservoir rocks.

Therefore the previously described complex physics justify the development of new numerical algorithms. As the equations are strongly nonlinear and fully coupled, an explicit iterative finite difference scheme is used. The steady state is reached by performing pseudo-transient nonlinear iterations, until convergence is reached. Then, the physical time is updated and the next time step is solved. The advantages of this numerical method are the straightforward implementation of the equations as well as light and performing codes, which do not require heavy memory access or matrices storage. The major limitation is the requirement of a more restrictive time step, in comparison to other

implicit methods. The benefits of such an implementation have no big influence for 1D runs, but become highly interesting and needed while going to two- or three-dimensional (3D) setups. High resolution in both space and time of our models is essential to capture the multi-scale and spontaneous fluid focusing events caused by dynamic porosity and accompanying permeability increase. Conventional resolution, much lower than characteristic compaction length, would simply miss these events. Such runs can only be produced on massively parallel supercomputing architectures, using latest technologies, such as graphical processing units (GPU) and many integrated core architectures (MICs). The inherent low-level parallelism of explicit methods justifies in itself the development of new algorithms, scaling linearly and performing very well on all tested machines.

3.1. Numerical setup of the model

Two different setups were investigated, in various spatial dimensions. The 1D and 3D runs have the same setup, while the 2D runs explored a more complex geometry closer to a reservoir setting. The first setup, used in the 1D and 3D runs, is an initial Gaussian porosity perturbation located at ¼ of the domain height, standing for an injection pulse. Total pressure and fluid pressures are initialized in order to set effective pressure on the neutral line within the failure envelope.

The 2D run (Fig. 2), contains nine shale layers, reproducing Sleipner's geometry, but the properties of the layers differ in porosity and permeability only. Injection is performed from the bottom of the model. Within the 1D runs (Fig. 3), we compare two major different rock types found in the Sleipner reservoir, with unconsolidated sandstones constituting the main reservoir rock and the shale forming the low-permeability layers. Values for important parameters used in this setup can be found in Table 1. Finally, the 3D runs (Figs. 4 and 5) focus on the nontrivial stress distribution and effect of horizontal shear stress on the wave propagation and geometry.

Table 1. Parameters used for 1D runs in shale and sandstone rocks.

	Shale	Sandstone	Units
Bulk viscosity	1e11	1e14	[Pa s]
Permeability	2e-6	2	[Darcy]
Brine+CO_2 viscosity	8e-4	8e-4	[Pa s]
Brine+CO_2 density	1020	1020	[kg m^{-3}]

Note: Values from [35, 40, 41, 44].

4. Results and discussion

4.1. Fluid flow in deforming rocks and channel formation

Simon and co-workers [30, 45] have previously presented 2D simulation results on fluid injection into viscoelastoplastically deforming rocks using a simplified mechanical approach following [46]. The simplification is that total pressure is considered to be lithostatic. In addition, solid velocities were assumed to be small compared to fluid velocities and set to zero. Stresses, and in particular deviatoric stresses, were therefore not calculated and the deformation of the solid matrix could not be simulated. In addition, Biot poro-elasticity was not included. An example for a 2D simulation of flow in a layered reservoir is given in Figure 2 (from [30]). The run is initialized with a high porosity and permeability background with 9 interspersed low porosity and permeability layers, and some random heterogeneity. Initial pressure is uniform (lithostatic). The layers are discontinuous and the box is open at the sides, so fluid can escape sideways. Fluid injection occurs in the light blue squares at the bottom of the box. Fluid flow is driven by buoyancy and local pressure gradients that develop due to fluid flow and deformation. High porosity channels (porosity waves) develop spontaneously and fluid breaches the initial low permeability layers (dark blue boxes, arrows). Note the strongly heterogeneous and dynamically changing pressure distribution, which differs significantly from pressure distribution predicted from flow simulations that do not include viscous deformation.
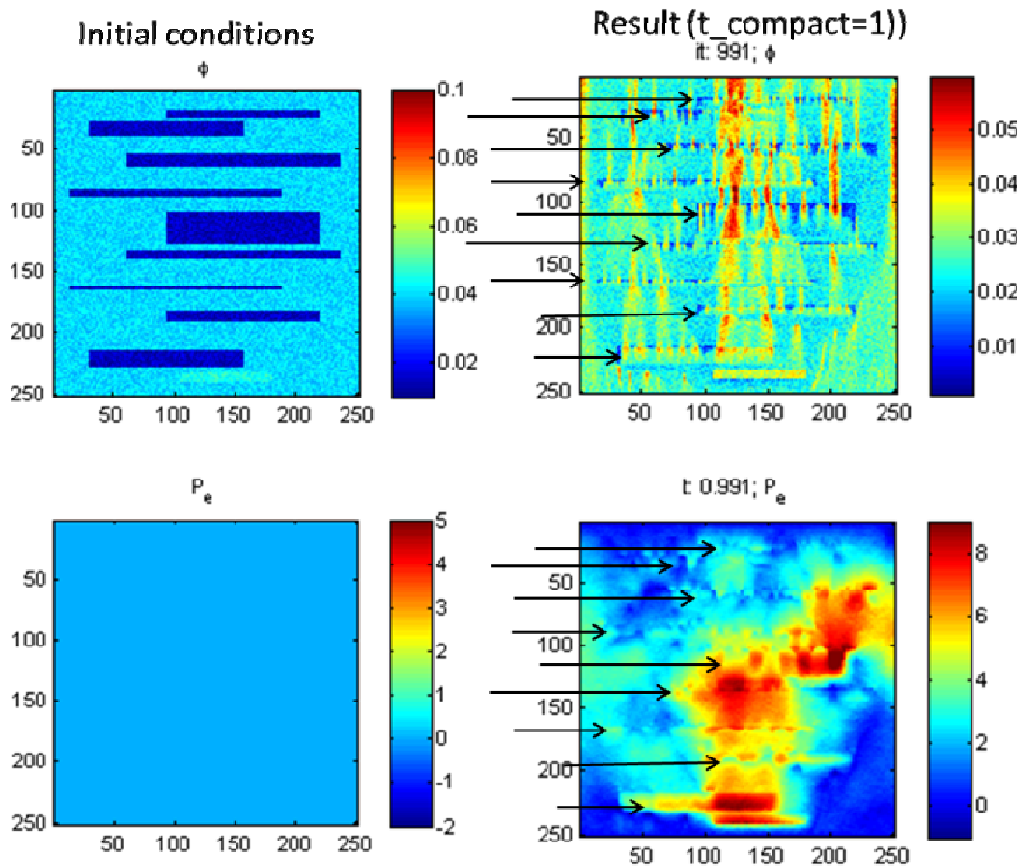
Fig. 2: Example of a 2-D (x, depth) simulation of fluid flow through a high permeability reservoir with interbedded low-permeability shales. The two left panels show initial condition for porosity (top) and effective pressure P_{total}-P_{fluid}= $\overline{p} - p^{f}$ (bottom). The right panels show results after one compaction time scale. Arrows indicate locations of the shale layers. Fluid is injected at the bottom of the reservoir. Sand and shale differ in porosity and permeability only, but have the same bulk viscosity and compressibility. All parameters are dimensionless. Model resolution is 251x251 grid cells. From [30].

4.2. Model development, improvements and goals

Our new model includes full mechanics as described in section 2. In addition, the code has been extended to three dimensions, see section 3. These improvements allow to accurately model fluid injection and flow into heterogeneously stressed rocks. In addition, non-linear stress dependent rheology is included, which may play a crucial role for mechanical weakening of the rock, the opening of pore space and the onset of failure [47-50]. Ultimately, the model will allow us to i) compute speed and direction of fluid flow in a pre-stressed subsurface, the feedback on solid stresses and the deformation including surface deformation, ii) explore the onset of failure of preexisting and new faults and fractures, iii) determine the conditions for channelized flow and iv) constrain operating parameters for CO_2 injection to assure storage containment and integrity over time. As we show in this

1. *unconsolidated sandstone rheology*
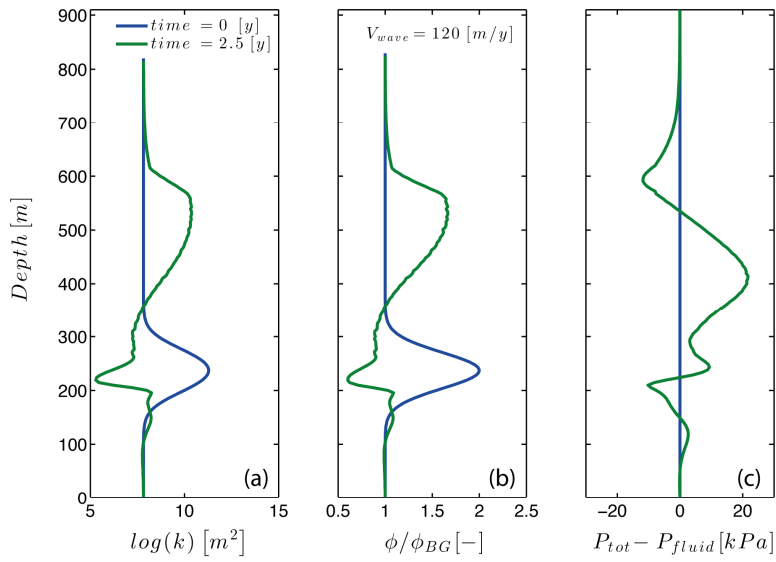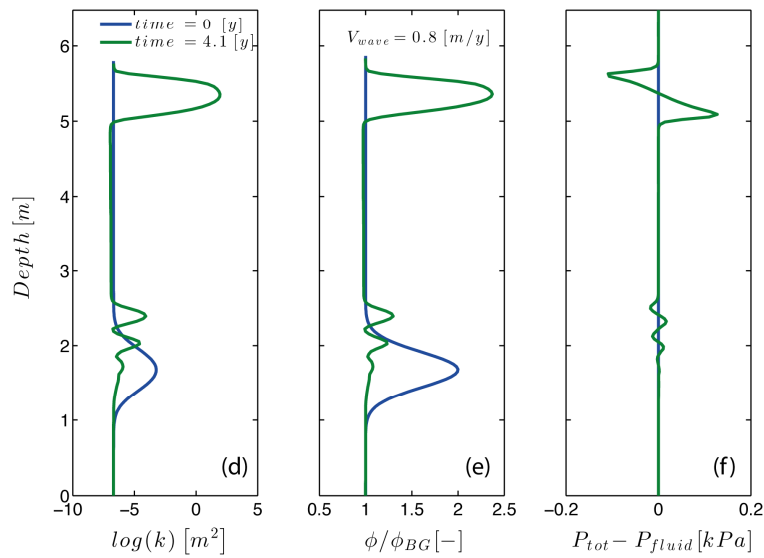
2. *shale rheology*

Fig. 3: Formation and evolution of high-permeability regions traveling upwards in unconsolidated sandstone (upper panel) and shale (lower panel). Logarithmic permeability (a, d), porosity normalized to background porosity (b, e) and effective pressure (P_{total}-P_{fluid}= $\overline{p} - p^f$; c, f) are shown for the initial condition (t=0, blue line) and some later time (green line; 2,5 years and 4,1 years for sandstone and shale, respectively). Else, both runs have identical initial and boundary conditions as described in the text and given in Table 1. Note the different scales for height of the wave, permeability and pressure in the two rock types.

paper, localized flow due to viscoplastic deformation is likely to occur in reservoirs, and including complex rheology is crucial to predict localized flow phenomena other than brittle failure.

4.3. Porosity waves in 1-D and the effect of rock properties

In this section we explore fluid movement in two rock types that are common and representative for CO_2 storage aquifers and cap rocks, respectively, namely loosely consolidated sand (such as the Utsira sand and Sleipner or the Mount Simon sandstone in Illinois) and shale. Mechanical and petrophysical properties of these rock types are taken from the literature, see Table 1. Figure 3 shows two examples for unconsolidated sandstone rheology and typical shale rheology. The high-porosity, high-permeability sandstone (k_0 = 2 Darcy) was chosen to have a power law exponent n=5 for porosity-dependent permeability (equation (15)) and a solid viscosity η_s=1*10^{13} Pas. The low permeability shale in turn has n=15 and η_s=1*10^{11} Pas. The two runs were otherwise initialized identically, as described in section 3.1.

Both runs result in the formation of a porosity wave that travels upward, but the characteristic length and time scales as well as the shapes of the waves differ significantly for the two rock types. The wave travels faster in the sandstone (120 *m/y* vs. 0.8 *m/y* in the shale; Fig. 3 b and e), but is much more elongated (height ~250 m with correspondingly large width) with maximum amplitudes in both porosity and permeability that are lower than the amplitude of the initial perturbation. In the shale, in contrast, the wave is much more focused (height ~1 m, implying a similar or smaller width, see 2D and 3D calculations). Moreover, the maximum amplitude of porosity and permeability increases during upward travel of the fluid-filled perturbation in the shale. Thus, more fluid is concentrated in a smaller volume in the shale while fluid is distributed over a larger depth range in the sandstone. In 3D, the porosity wave would look more like a large blob or plume in the sandstone, while it looks more like a crack or channel in the shale.

The perturbations in effective pressure are significantly larger in the sandstone compared to the shale due to the lower viscosity in the shale. I.e., less effective pressure is needed to open and close pore space in the shale because it is softer. This also implies that a pressure pulse associated to a porosity wave traveling through sandstone is easily large enough to cause deformation and pore opening in a soft shale that is interspersed or overlying a sandstone. Since the velocity of the fluid and the amplitude of the wave are much higher in the sandstone than in the shale, some lateral spreading of fluid underneath shale layers is expected.

4.4. Examples of 3D simulations

The results of the previous 2D modeling [30] were confirmed and extended by 3D calculations. Numerical runs with the newly developed 3D hydromechanical simulator show that parallel GPU programming allows for fast runs of fully coupled numerical algorithms with high resolution in 3D. Localized upward fluid propagation previously predicted with 2D simulations was also observed in 3D (Figs. 4 and 5). Fig. 4 shows the propagation of an initially spherical CO_2 plume in a viscoelastic porous rock subjected to background shear stresses. No flux boundary conditions are imposed. Buoyancy force generates high fluid overpressures at the top of the plume leading to non-homogeneous distributions of fluid and total pressures (left columns in Fig. 4). High fluid overpressures at the top dilate the pores pushing CO_2 upwards and generating local variations in shear stresses as shown at the right columns in Fig. 4. Since viscosity is non-linearly related to shear stress viscosity is reduced in high stress regions around the traveling plume [48]. This viscosity reduction leads to higher propagation speed, even without invoking plasticity. However, variations in shear stress might eventually lead to failure or reactivation of pre-existing faults, when the critical yield stress is reached. This scenario is investigated in Fig. 5 where we assume that effective viscosity reduces with decreasing effective pressure at the onset of failure (see Fig. 1), and also shown in Fig. 2. As a result viscosity of the reservoir rock is different at the top of the propagating plume and at its bottom. Therefore, pores that were pushed open when the plume first reached them do not recover their initial volume. This leads to formation of vertical channels that are able to propagate upwards much faster than spherical blobs [51].
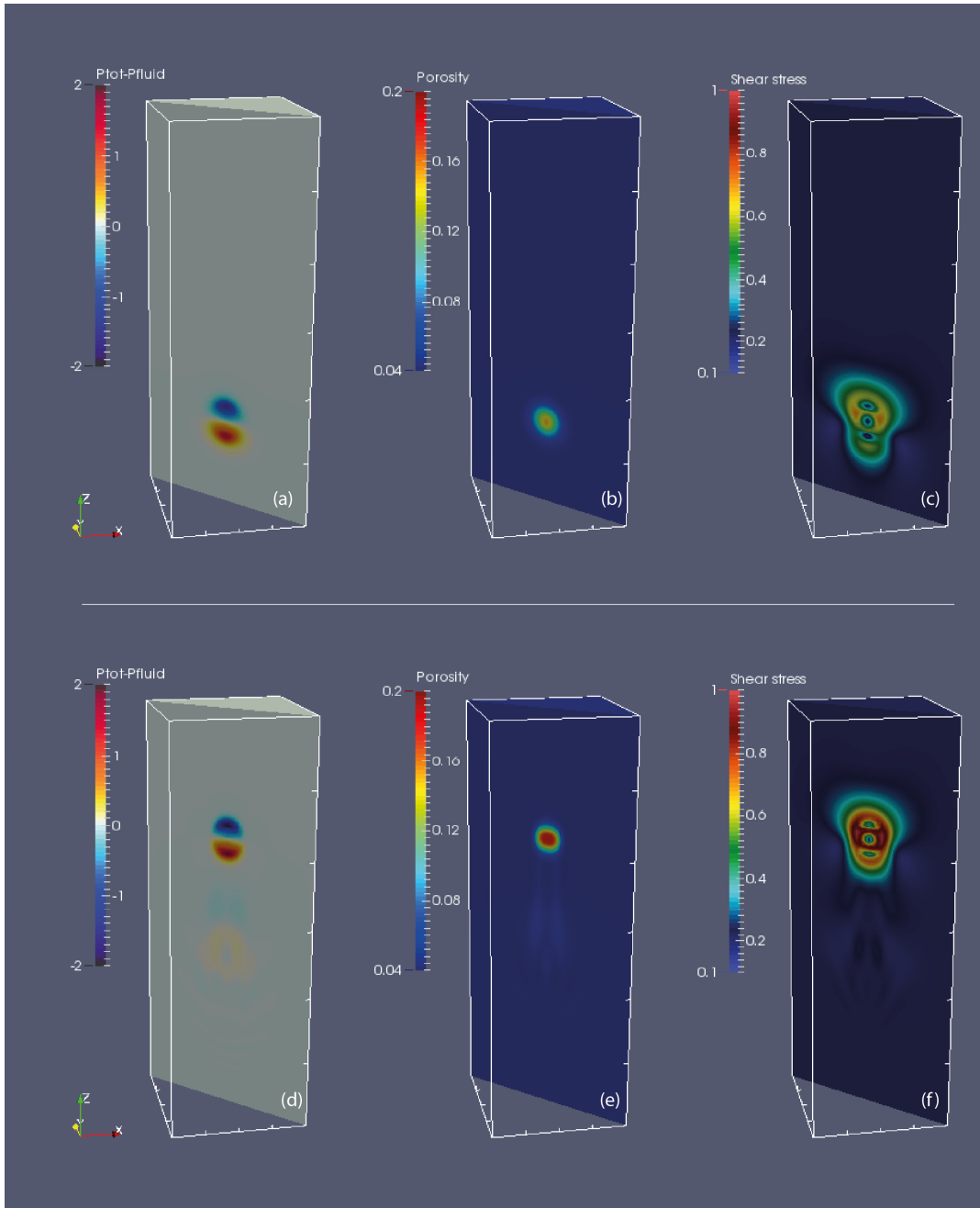
Fig. 4: Three dimensional (3D) numerical simulation results of propagating porosity perturbation through nonlinear viscous porous rock, exposed to background shear stress. Initial porosity perturbation is implemented as an 3D Gaussian, located at Lz/4 and with amplitude equal to three times the background porosity. Subplots shown for dimensionless time steps 1 (a, b, c) and 80 (d, e, f) are, respectively, the effective pressure (P_{total}-P_{fluid}= $\overline{p} - p^{f}$; (a, c)), the porosity distribution (b, d) and the shear stress invariant (c, e). All dimensionless parameters.
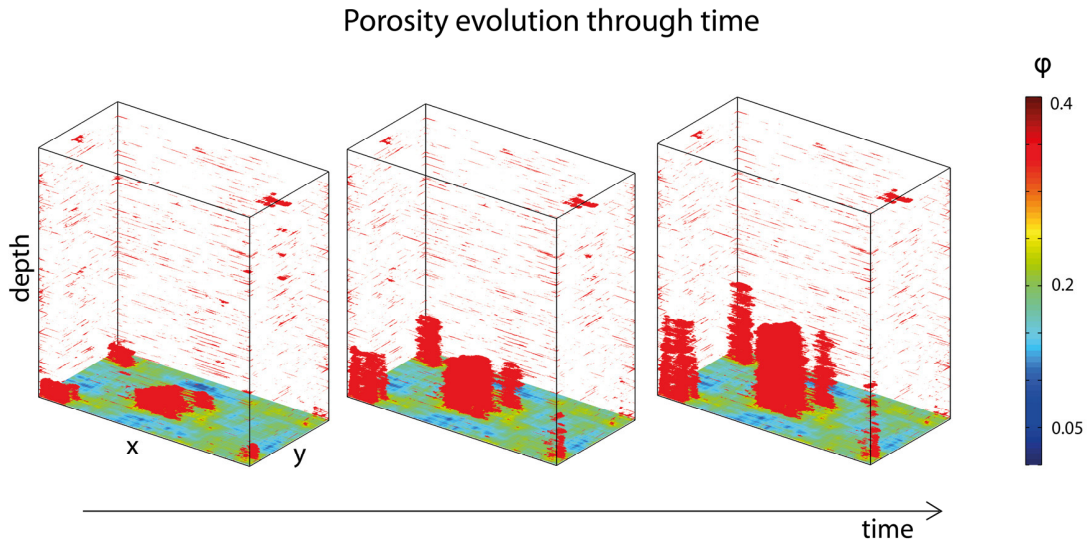
Porosity evolution through time

Fig. 5: Porosity evolution from high-resolution 3D simulation of focusing two-phase flow analogous to the 2D simulation presented in Fig. 2. 480 x 240 x 480 grid points resolution in (x,y,z) dimensions, performed with C-CUDA and MPI on 4 GPUs. Full mechanics, bilinear viscosity and XY Gaussian trended background randomness [52].

5. Conclusions

- We developed a new 3D fully coupled numerical algorithm for fluid flow in deforming poroviscoelastoplastic rocks.
- The implemented rheology accounts for three different types of non-linearities: Asymmetry in compaction and decompaction, porosity dependent bulk properties and viscosity that depends non-linearly on shear stresses.
- The new model predicts the formation of self-propagating high-porosity channels as an essential feature
- Resolving channel formation requires high spatial and temporal resolution, which requires high-performance computing.
- Deduced time and length scales for CO_2 upward migration are in agreement with observations from the Sleipner CO_2 storage pilot.
- Time dependent rheology and non-linear porosity-dependent permeability have a major impact on deformation and flow. Thus, they have to be included in numerical codes in order to obtain reliable simulations of CO_2 injection and storage operations.

Acknowledgements

References

[1] IEA, Technology Roadmap - Carbon capture and storage, 2013 edition, in: I.E. Agency (Ed.) TEchnology Roadmap, Paris, 2013, pp. 59.
[2] E.K. Halland, W.T. Johansen, F. Riis, CO2 Storage Atlas: Norwegian North Sea, in, The Norwegian Petroleum Directorate, Stavanger, Norway, 2011.

[3] E.K. Halland, W.T. Johansen, F. Riis, CO2 Storage Atlas: Norwegian Sea, in, The Norwegian Petroleum Directorate, Stavanger, Norway, 2013.

[4] R.A. Chadwick, D.J. Noy, Achieving regulatory conformance: a study in prediction and verification at Sleipner, in: 7th TCCS, Trondheim, Norway, 2013.

[5] A.J. Cavanagh, R.S. Haszeldine, The Sleipner storage site: Capillary flow modeling of a layered CO2 plume requires fractured shale barriers within the Utsira Formation, Int. J. Greenhouse Gas Cont., 21 (2014) 101-112.

[6] J. Rutqvist, The Geomechanics of CO2 Storage in Deep Sedimentary Formations, Geotech Geol Eng, 30 (2012) 525-551.

[7] J.F. Harrington, D.J. Noy, S.T. Horseman, D.J. Birchall, R.A. Chadwick, Laboratory study of gas and water flow in the Nordland Shale, Sleipner, North Sea, in: M. Grobe, J.C. Pashin, R.L. Dodge (Eds.) Carbon dioxide sequestration in geological media-State of the science, 2009, pp. 521- 543.

[8] R.A. Chadwick, D.J. Noy, History-matching flow simulations and time-lapse seismic data from the Sleipner CO2 plume, Geological Society, London, Petroleum Geology Conference series, 7 (2010) 1171-1182.

[9] S.T. Horseman, J.F. Harrington, P. Sellin, Gas migration in clay barriers, Eng Geol, 54 (1999) 139-149.

[10] A.E. Ortiz R, J. Renner, R. Jung, Hydromechanical analyses of the hydraulic stimulation of borehole Basel 1, Geophys J Int, 185 (2011) 1266-1287.

[11] S.E. Ingebritsen, C.E. Manning, Permeability of the continental crust: dynamic variations inferred from seismicity and metamorphism, Geofluids, 10 (2010) 193-205.

[12] I.G. Main, L. Li, K.J. Heffer, O. Papasouliotis, T. Leonard, Long-range, critical-point dynamics in oil field flow rate data, Geophys. Res. Lett., 33 (2006) L18308.

[13] A. Nermoen, O. Galland, E. Jettestuen, K. Fristad, Y. Podladchikov, H. Svensen, A. Malthe-Sørenssen, Experimental and analytic modeling of piercement structures, J. Geophys. Res., 115 (2010) B10202.

[14] A.Y. Rozhko, Y.Y. Podladchikov, F. Renard, Failure patterns caused by localized rise in pore-fluid overpressure and effective strength of rocks, Geophys Res Lett, 34 (2007) doi:10.1029/2007GL031696.

[15] S. Baisch, R. Voros, E. Rothert, H. Stang, R. Jung, R. Schellschmidt, A numerical model for fluid injection induced seismicity at Soultz-sous-Forets, Int. J. Rock Mech. Mining Sci., 47 (2010) 405-413.

[16] X.-Z. Kong, W. Kinzelbach, F. Stauffer, Migration of air channels: An instability of air flow in mobile saturated porous media, Chemical Engineering Science, 64 (2009) 1528-1535.

[17] J.A.D. Connolly, Y.Y. Podladchikov, Temperature-dependent viscoelastic compaction and compartmentalization in sedimentary basins, Tectonophys., 324 (2000) 137-168.

[18] V.M. Yarushina, (De-)compaction waves in porous viscoelastoplastic media, in: Faculty of Mathematics and Natural Sciences, University of Oslo, Oslo, 2009, pp. 165.

[19] E. Tantserev, C.Y. Galerne, Y.Y. Podladchikov, Multiphase Flow in Multi-Component Porous Visco-Elastic Media, in: H.I. Ling, A. Smyth, R. Betti (Eds.) 4th Biot Conference on Poromechanics, Destech Publications, Inc, New York, NY, 2009, pp. 959-964.

[20] M.S. Appold, J.A. Nunn, Numerical models of petroleum migration via buoyancy-driven porosity waves in viscously deformable sediments, Geofluids, 2 (2002) 233-247.

[21] Y. Le Guen, F. Renard, R. Hellmann, E. Brosse, M. Collombet, D. Tisserand, J.P. Gratier, Enhanced deformation of limestone and sandstone in the presence of high PCO2 fluids, J. Geophys. Res., 112 (2007) B05421.

[22] D. Elsworth, H. Yasuhara, Short-Timescale Chemo-Mechanical Effects and their Influence on the Transport Properties of Fractured Rock, Pure Appl. Geophys., 163 (2006) 2051-2070.

[23] J. Taron, D. Elsworth, Coupled mechanical and chemical processes in engineered geothermal reservoirs with dynamic permeability, Int. J. Rock Mech. Mining Sci., 47 (2010) 1339-1348.

[24] V.M. Yarushina, D. Bercovici, Mineral carbon sequestration and induced seismicity, Geophys Res Lett, 40 (2013) 814-818.

[25] P.N. Hagin, M.D. Zoback, Viscous deformation of unconsolidated reservoir sands—Part 2: Linear viscoelastic models, Geophysics, 69 (2004) 742-751.

[26] H. Sone, M.D. Zoback, Visco-plastic properties of shale gas reservoir rocks, in: 45th US Rock Mechanics / Geomechanics Symposium, American Rock Mechanics Association, San Francisco, CA, 2011, pp. ARMA 11-417.

[27] M.D. Zoback, S.M. Gorelick, Earthquake triggering and large-scale geologic storage of carbon dioxide, P Natl Acad Sci USA, 109 (2012) 10164-10168.

[28] M.D. Zoback, Reservoir geomechanics, 2nd ed., Cambridge University Press, Cambridge, 2010.

[29] N.S.C. Simon, Y.Y. Podladchikov, A Consistent Physical Model Predicting the Formation of Focused Flow Channels - Application to CO2 Injection at Sleipner, in: Second SES Conference, EAGE, Pau, France, 2013, pp. 4.

[30] N.S.C. Simon, Y.Y. Podladchikov, A consistent physical model for the formation of focused flow channels (chimneys) through intra-reservoir shales, in: The 7th Trondheim CCS Conference (TCCS-7), Trondheim, Norway, 2013.

[31] N.S.C. Simon, Compaction Driven Flow in Porosity Waves - A Threat to Caprock Integrity?, in: Third EAGE CO2 Geological Storage Workshop - Understanding the Behaviour of CO2 in Geologic Storage Reservoirs, EAGE, Edinburgh, UK, 2012, pp. 12288.

[32] N.S.C. Simon, Fluid focusing and breaching of low permeability layers in reacting and visco-elasto-plastically deforming reservoir rocks, Geophysical Research Abstracts, 15 (2013) EGU2013-5865.

[33] V.M. Yarushina, Y.Y. Podladchikov, (De)compaction of porous viscoelastoplastic media: 1. Thermodynamically admissible model formulation, J Geophys Res, (2014).

[34] H.F. Wang, Theory of Linear Poroelasticity with Applications to Geomechanics and Hydrogeology, Princeton University Press, 2000.

[35] J.-J. Dong, J.-Y. Hsu, W.-J. Wu, T. Shimamoto, J.-H. Hung, E.-C. Yeh, Y.-H. Wu, H. Sone, Stress-dependence of the permeability and porosity of sandstone and shale from TCDP Hole-A, Int. J. Rock Mech. Mining Sci., 47 (2010) 1141-1157.

[36] C. David, T.-F. David, W. Wong, J. Zhu, Zhang, Laboratory measurement of compaction-induced permeability change in porous rocks: Implications for the generation and maintenance of pore pressure excess in the crust, Pure Appl. Geophys., 143 (1994) 425-456.

[37] D. McKenzie, The Generation and Compaction of Partially Molten Rock, Journal of Petrology, 25 (1984) 713-765.

[38] D.M. Audet, A.C. Fowler, A mathematical model for compaction in sedimentary basins, Geophys J Int, 110 (1992) 577-590.

[39] V. Barcilon, F.M. Richter, Nonlinear-waves in compacting media, Journal of Fluid Mechanics, 164 (1986) 429-448.

[40] H. Sone, M.D. Zoback, Time-dependent deformation of shale gas reservoir rocks and its long-term effect on the in situ state of stress, Int. J. Rock Mech. Mining Sci., 69 (2014) 120-132.

[41] P.N. Hagin, M.D. Zoback, Viscous deformation of unconsolidated sands—Part 1: Time-dependent deformation, frequency dispersion, and attenuation, Geophysics, 69 (2004) 731-741.

[42] J. Rutqvist, Status of the TOUGH-FLAC simulator and recent applications related to coupled fluid flow and crustal deformations, Comput Geosci-Uk, 37 (2011) 739-750.

[43] J.H. Prevost, Two-way coupling in reservoir-geomechanical models: vertex-centered Galerkin geomechanical model cell-centered and vertex-centered finite volume reservoir models, Int J Numer Meth Eng, 98 (2014) 612-624.

[44] A. Cavanagh, Benchmark Calibration and Prediction of the Sleipner CO2 Plume from 2006 to 2012, Energy Procedia, 37 (2013) 3529–3545.

[45] N.S.C. Simon, L. Räss, Y.Y. Podladchikov, A. Souche, V.M. Yarushina, Predicting dynamically evolving permeability and localization of fluid flow in underground waste storage operations, in: EAGE International Workshop on Geomechanics and Energy, EAGE, Lausanne, Switzerland, 2013, pp. extended abstract.

[46] J.A.D. Connolly, Y.Y. Podladchikov, Compaction-driven fluid flow in viscoelastic rock, Geodinamica Acta, 11 (1998) 55-84.

[47] R.P. Chhabra, Bubbles, drops, and particles in non-Newtonian fluids, 2nd ed., Taylor and Franics, Boca Raton, 2007.

[48] L. Räss, Three-Dimensional GPU-Accelerated Modelling of Buoyancy-Driven Flow under Horizontal Far-Field Stress, in: Institute of Earth Science, University of Lausanne, Lausanne, 2013, pp. 77.

[49] L. Räss, S. Omlin, Y. Podladchikov, Influence of intrinsic and extrinsic forces on 3D stress distribution using CUDA programming, Geophysical Research Abstracts, 15 (2013) EGU2013-12637.

[50] V.M. Yarushina, D. Bercovici, M.L. Oristaglio, Rock deformation models and fluid leak-off in hydraulic fracturing, Geophys J Int, 194 (2013) 1514-1526.

[51] J.A.D. Connolly, Y.Y. Podladchikov, Decompaction weakening and channeling instability in ductile porous media: Implications for asthenospheric melt segregation, Journal of Geophysical Research, 112 (2007) doi:10.1029/2005JB004213.

[52] L. Räss, S. Omlin, E. Moulas, N.S.C. Simon, Y. Podladchikov, Multi-GPU Accelerated Simulation of Dynamically Evolving Fluid Pathways, in: EGU General Assembly 2014, Vienna, Austria, 2014.